photonics

MDPI

Article

Counterdiabatic Driving for Fast Quantum Control with Asymmetric Pulses

Mengmeng Yuan [1,2], Xinbo Li [1,2], Haozhe Wang [2], Xu Zhao [2], Zhenqi Bai [2,3], Min Feng [2,3], Ruyue Guo [2,3] and Yichi Zhang [2,3,*]

[1] Sanli Honors College, School of Physics and Electronics Engineering, Shanxi University, Taiyuan 030006, China; yuanmengmeng@sxu.edu.cn (M.Y.); lixinbo2@sxu.edu.cn (X.L.)
[2] College of Physics and Electronic Engineering, Shanxi University, Taiyuan 030006, China; wanghaozhe@sxu.edu.cn (H.W.); zhaoxu1@sxu.edu.cn (X.Z.); baizhenqi@sxu.edu.cn (Z.B.); fengmin2@sxu.edu.cn (M.F.); guoruyue@sxu.edu.cn (R.G.)
[3] Collaborative Innovation Center of Extreme Optics, Shanxi University, Taiyuan 030006, China
* Correspondence: zhangyichi@sxu.edu.cn

Abstract

Fast quantum control with asymmetric pulses is constrained by nonadiabatic transitions generated at rapidly varying pulse edges. Here, we combine rapidly turned-on and slowly turned-off (RTST) and slowly turned-on and rapidly turned-off (STRT) pulse sequences with counterdiabatic driving in a semiclassical two-level system to achieve population transfer from the initial state |1> to the target state |2>, with fast-edge durations ranging from 0.1 to 0.8 ps (100–800 fs). The asymmetric pulse shapes allow independent control of the rising and falling edges, while a counterdiabatic correction constructed from the adiabatic gauge potential suppresses residual nonadiabatic coupling. Without counterdiabatic correction, the optimized RTST and STRT sequences yield final target-state populations of 99.984% and 98.173%, respectively, and retain their characteristic population dynamics in the presence of spontaneous decay. With counterdiabatic driving, the final target-state fidelity exceeds 0.99999 for both protocols over a broader range of the considered control parameters. These results demonstrate that counterdiabatic driving effectively compensates fast-edge-induced nonadiabaticity, enabling fast and high-fidelity quantum control with asymmetric pulses.

Keywords: asymmetric pulses; counterdiabatic driving; shortcuts to adiabaticity; adiabatic gauge potential; population transfer; quantum control

1. Introduction

With the rapid development of quantum technology, precise and efficient control of quantum systems has become a key requirement for advances in quantum computing, quantum simulation, and other frontier fields [1–5]. Adiabatic evolution is a well-established approach to controlling quantum dynamics [6–8]. By varying the parameters of the driving Hamiltonian sufficiently slowly, undesired excitations can be suppressed, allowing the system wave function to remain close to the corresponding instantaneous eigenstate throughout the evolution. Adiabatic methods, such as rapid adiabatic passage (RAP) and stimulated Raman adiabatic passage (STIRAP) [9–14], have been applied to both two-level and multilevel systems, demonstrating the stability and robustness of adiabatic control. Extensions of adiabatic population transfer to multistate molecular systems and pulse-train control have further demonstrated efficient population manipulation, while studies of extended systems have also clarified the limitations of STIRAP robustness in the presence of background-state couplings [15–17].

Check for updates

Received: 9 October 2026
Revised: 11 November 2026
Accepted: 16 November 2026
Published: 18 November 2026

Copyright: © 2026 by the authors. Licensee MDPI, Basel, Switzerland. This article is an open access article distributed under the terms and conditions of the Creative Commons Attribution (CC BY) license.

However, conventional adiabatic operations, although robust in controlling the final state and resistant to parameter fluctuations, still face important practical limitations. Their slow operation reduces efficiency in tasks requiring high repetition rates [18,19]. For example, in quantum-information protocols based on ion or atom transport, excessively long operation times can limit practical feasibility [20–22]. In addition, long operation times expose quantum systems to decoherence, noise, and dissipative processes for extended periods [23]. Therefore, accelerating the operation while maintaining high control fidelity is an important objective in practical quantum control [24].

To overcome the time bottleneck of adiabatic processes, shortcuts to adiabaticity (STA) [25,26] have attracted considerable attention in recent years. STA includes counterdiabatic driving [27–29], inverse engineering [30–34], fast-forward methods [35,36], and optimal control theory [37–40]. The central goal of STA is to eliminate or suppress nonadiabatic transitions between the instantaneous eigenstates of the Hamiltonian, allowing the system to evolve from the initial state to the target state more rapidly while retaining adiabatic-like dynamics. Among these approaches, counterdiabatic driving (CD), also known as transitionless quantum driving, was independently proposed by Berry [41], while Demirplak and Rice developed the counterdiabatic-field formulation in a series of works [42–44]. As one of the most actively studied STA approaches, CD introduces an auxiliary term into the Hamiltonian to cancel nonadiabatic transitions and force the system to follow the reference adiabatic path, thereby providing a new route to overcome the timescale limitation of conventional adiabatic operations. This approach has been widely investigated and applied both theoretically and experimentally [45–50]. A key element of this compensation mechanism is the adiabatic gauge potential (AGP). By providing a real-time correction associated with the time dependence of the Hamiltonian, the AGP reduces the probability of nonadiabatic transitions to a low level and, in principle, enables equivalent adiabatic control over arbitrarily short timescales. CD plays an important role in studies of quantum dynamics on timescales shorter than the decoherence time and offers advantages for population transfer, quantum many-body dynamics, quantum computing, and quantum simulation.

In current studies, smooth laser pulses, such as Gaussian-shaped and chirped pulses, are commonly used to drive quantum systems. Their smooth and symmetric rising and falling edges keep the time derivative of the Hamiltonian, $\partial H/\partial t$, relatively small, which helps satisfy the conditions required for adiabatic evolution. As a result, such pulse shapes generally provide good robustness and high fidelity in quantum control [51–54]. Despite these advantages, the inherent time-bandwidth product of symmetric pulses limits the extent to which the total pulse duration can be reduced when high spectral selectivity, corresponding to a narrow bandwidth, is required. More importantly, the symmetric temporal profiles of the rising and falling edges restrict the independent optimization of the temporal characteristics of different stages, thereby limiting the possibility of further accelerating specific stages of the transfer process.

To overcome the limited temporal flexibility of symmetric pulses while retaining the advantages of smooth evolution, asymmetric pulse designs, such as slowly turned-on and rapidly turned-off (STRT) pulses and rapidly turned-on and slowly turned-off (RTST) pulses, provide an attractive alternative [55,56]. These pulse shapes allow the rise and fall times to be controlled independently, enabling targeted optimization of different stages of the transfer process.

In the STRT pulse sequence, the slow turn-on helps the system satisfy the adiabatic condition during the initial stage of the transfer, thereby minimizing initial nonadiabatic transitions and improving the fidelity of the intended transfer pathway. The rapid turn-off acts near the end of the transfer and is intended to lock the final-state population, suppress

back-transfer, and minimize decoherence or population loss caused by continued laser irradiation, thereby maximizing and stabilizing the final population accumulation [56]. In contrast, the rapid turn-on of the RTST pulse sequence quickly establishes the coupling and significantly shortens the time required for the system to enter the adiabatic transfer path. It also reduces the time over which nonadiabatic effects can accumulate during the initial stage, thereby accelerating the overall adiabatic-transfer process. The slow turn-off then provides more time for smooth and stable evolution as the transfer approaches completion, promoting efficient and more complete population accumulation in the target state and helping to achieve a higher final-state population. Although asymmetric pulses, especially their fast edges, can significantly shorten the operation time, their relatively steep temporal variation can introduce residual nonadiabatic transitions, constituting a bottleneck for the final robustness and fidelity [57].

To address this limitation, we propose a quantum-control strategy that combines asymmetric laser pulse sequences with counterdiabatic driving. In this approach, asymmetric pulse shaping provides temporal flexibility and allows the rising and falling edges to be independently optimized. The slow edge guides the system along an approximately adiabatic path, suppresses the dominant nonadiabatic errors. Meanwhile, the very short duration of the fast edge substantially shortens the overall control duration, meeting the requirements of ultrafast quantum operations. Counterdiabatic driving can then be constructed with respect to a prescribed reference Hamiltonian to compensate for the nonadiabatic coupling along the corresponding control path. In this way, near-ideal population-transfer fidelity can be maintained even during the fast-edge interval, providing a balance among operation speed, transfer fidelity, and control precision.

2. Theoretical Methods

We first consider a semiclassical model of a two-level quantum system interacting with a classical electric field. In the Schrödinger picture, the system Hamiltonian under the electric-dipole approximation is

$$H_s(t) = \begin{pmatrix} E_1 & V(t) \\ V^*(t) & E_2 \end{pmatrix}. \tag{1}$$

where $V(t) = -\langle 1|d|2\rangle \cdot E(t)$, E_1 and E_2 are the bare-state energies, and d is the dipole-moment operator. The time-dependent electric field of the asymmetric laser pulse sequence can be written as

$$E(t) = \sum_{i=1}^{N} E_0 f_i(t) \cos\{\omega_L[t - (i-1)T_R - t_0] + (i-1)\varphi\}. \tag{2}$$

where the field envelope $f_i(t)$ and the normalized intensity envelope $g_i(t)$ are related by

$$\begin{aligned} f_i^2(t) \equiv g_i(t) &= \exp\left[-\tfrac{[t-t_0-(i-1)T_R]^2}{\tau^2}\right], \\ \tau &= \begin{cases} \tau_r, & t_i^{\text{begin}} < t \le t_0 + (i-1)T_R, \\ \tau_f, & t_0 + (i-1)T_R < t < t_i^{\text{end}}. \end{cases} \end{aligned} \tag{3}$$

where E_0 is the field amplitude, t_0 is the time corresponding to the peak of the first pulse, ω_L is the carrier angular frequency, T_R is the repetition period, N denotes the total number of pulses, and φ is the phase difference between two adjacent pulses. τ_r and τ_f denote the rise and fall times, respectively. t_i^{begin} and t_i^{end} denote the beginning and end of the ith pulse. The pulse envelope is set to zero outside the interval $t_i^{\text{begin}} \le t \le t_i^{\text{end}}$. Here, we focus on two asymmetric pulse sequences, RTST and STRT, for comparative analysis; their envelope shapes are shown in Figure 1a,b.

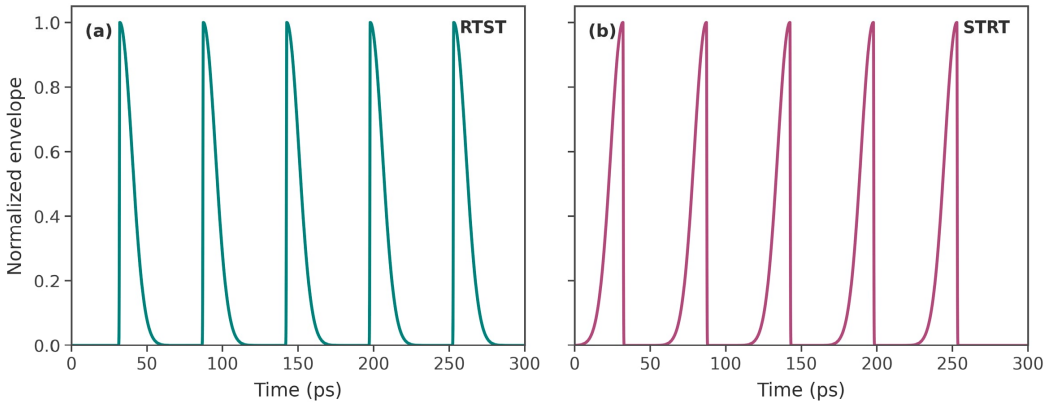


Figure 1. (**a**) Normalized field envelope of the RTST pulse sequence with parameters $\tau_r = 0.2$ ps, $\tau_f = 8$ ps, $t_0 = 32$ ps, $T_R = 55.24$ ps; (**b**) Normalized field envelope of the STRT pulse sequence with parameters $\tau_f = 0.2$ ps, $\tau_r = 8$ ps, $t_0 = 32$ ps, $T_R = 55.24$ ps.

To describe the time evolution of the two-level system, we use the Liouville–von Neumann equation,

$$i\hbar\dot{\rho} = [H(t), \rho]. \tag{4}$$

To account for spontaneous decay, the density-matrix dynamics are described by the Lindblad master equation

$$\dot{\rho} = -\frac{i}{\hbar}[H(t), \rho] + \gamma\left(L\rho L^{\dagger} - \frac{1}{2}\{L^{\dagger}L, \rho\}\right), \tag{5}$$

where $L = |1\rangle\langle 2|$ is the jump operator describing spontaneous emission, and γ denotes the spontaneous-decay rate. Here, $H(t)$ denotes the coherent Hamiltonian used in the corresponding evolution. The target-state population is

$$P_2(t) = \langle 2|\rho(t)|2\rangle. \tag{6}$$

To suppress nonadiabatic transitions induced by finite-time evolution, we introduce the counterdiabatic (CD) driving into the two-level system. The total Hamiltonian is written as

$$H(t) = H_0(t) + H_{\mathrm{CD}}(t). \tag{7}$$

where the counterdiabatic Hamiltonian is expressed through the adiabatic gauge potential (AGP),

$$H_{\mathrm{CD}}(t) = \hbar\dot{\lambda}A_{\lambda} \tag{8}$$

where $\lambda = \lambda(t)$ denotes the time-dependent parameters specifying the control trajectory of H_0.

For a reference Hamiltonian $H_0(\lambda)$, the off-diagonal part of the AGP can be written as

$$A_{\lambda} = -i\sum_{m\neq n}\frac{|m\rangle\langle m|\partial_{\lambda}H_0(\lambda)|n\rangle\langle n|}{(E_m - E_n)} \tag{9}$$

For the CD-assisted population-transfer protocol considered here, we choose the two-level reference Hamiltonian as

$$H_0(t) = \frac{\hbar}{2}\begin{pmatrix} -\Delta(t) & \Omega(t) \\ \Omega(t) & \Delta(t) \end{pmatrix} = \frac{\hbar}{2}[\Omega(t)\sigma_x - \Delta(t)\sigma_z] \tag{10}$$

Here, $\Omega(t)$ follows the RTST/STRT asymmetric pulse envelope defined above, whereas $\Delta(t)$ specifies the independently prescribed detuning trajectory. Accordingly, the control

parameters are $\lambda(t) = \{\Omega(t), \Delta(t)\}$. For the present two-level system, the corresponding counterdiabatic Hamiltonian takes the form [58]

$$H_{\mathrm{CD}}(t) = \frac{\hbar}{2}\Omega_{\mathrm{CD}}(t)\sigma_y \tag{11}$$

with

$$\Omega_{\mathrm{CD}}(t) = \frac{\Omega(t)\dot{\Delta}(t) - \Delta(t)\dot{\Omega}(t)}{\Omega^2(t) + \Delta^2(t)} \tag{12}$$

Because $\Omega_{\mathrm{CD}}(t)$ depends on both $\dot{\Omega}(t)$ and $\dot{\Delta}(t)$, the CD correction is not restricted to the Bézier sweep interval.

The corresponding phase-controlled laboratory-frame field is obtained through an exact time-dependent unitary transformation, without invoking the rotating-wave approximation. Alternative CD realizations based on modified Rabi-frequency and detuning controls have also been developed [59,60].

The finite-time detuning trajectory is generated using a cubic Bézier schedule $B(s) = 3s^2 - 2s^3$, with $s = (t - t_a)/(t_b - t_a)$ and $0 \le s \le 1$, corresponding to the control points $P_0 = P_1 = 0$ and $P_2 = P_3 = 1$. Within the sweep interval, the detuning is varied as $\Delta(t) = \Delta_0[1 - 2B(s)]$, connecting $+\Delta_0$ and $-\Delta_0$ with zero slope at both boundaries. Thus, the RTST/STRT envelope specifies $\Omega(t)$, while the Bézier interpolation specifies $\Delta(t)$. For the present calculations, the detuning amplitude is set to $\Delta_0 = 12$ rad/ps. The Bézier sweep parameters are $t_a = 134.48$ ps, $t_b = 160.48$ps for RTST, and $t_a = 122.48$ ps, $t_b = 148.48$ ps for STRT.

To quantify the deviation from the prescribed control trajectory, the instantaneous fidelity is defined as

$$F(t) = \langle \psi_{\mathrm{ad}}(t)|\rho(t)|\psi_{\mathrm{ad}}(t)\rangle. \tag{13}$$

where $|\psi_{\mathrm{ad}}(t)\rangle$ is the instantaneous lower-energy eigenstate of $H_0(t)$. The final target-state fidelity is $F_{\mathrm{target}} = P_2(T)$.

3. Results

For the numerical calculations, the baseline pulse parameters are $E_0 = 1.0$ and $\omega_L = 2.5$ rad/ps for RTST, and $E_0 = 1.68$ and $\omega_L = 4.107$ rad/ps for STRT, where E_0 is expressed in effective coupling units. The common parameters are $t_0 = 32$ ps, $T_R = 55.24$ ps, and $N = 5$. The inter-pulse phase difference is $\varphi = \omega_L T_R \pmod{2\pi}$, giving approximately 6.153 rad and 0.676 rad for RTST and STRT, respectively. The pulse peaks are located at $t_i = t_0 + (i-1)T_R$, within the 300 ps evolution window.

Figure 2a shows the target-state population as a function of τ_r for the RTST pulse sequence, with the slow fall time τ_f fixed and the fast rise time τ_r optimized. The laser parameters were optimized as $\tau_f = 8$ ps, $t_0 = 32$ ps, $T_R = 55.24$ ps and $N = 5$. The fast rise time τ_r was scanned from 0.1 ps to 0.8 ps. The two curves show the maximum population reached during the evolution and the final target-state population after the laser pulse sequence ($t = 300$ ps), respectively. Our main focus is the final target-state population. For τ_r between 0.2 ps and 0.5 ps, the final population remains at a relatively high level. The maximum final population reaches 99.984% at approximately $\tau_r = 0.40$ ps. This behavior is physically expected. In the RTST sequence, the slow turn-off of the optical field allows the coupling to decrease gradually, thereby reducing residual population oscillations and nonadiabatic leakage and helping to retain the accumulated population in the target state.

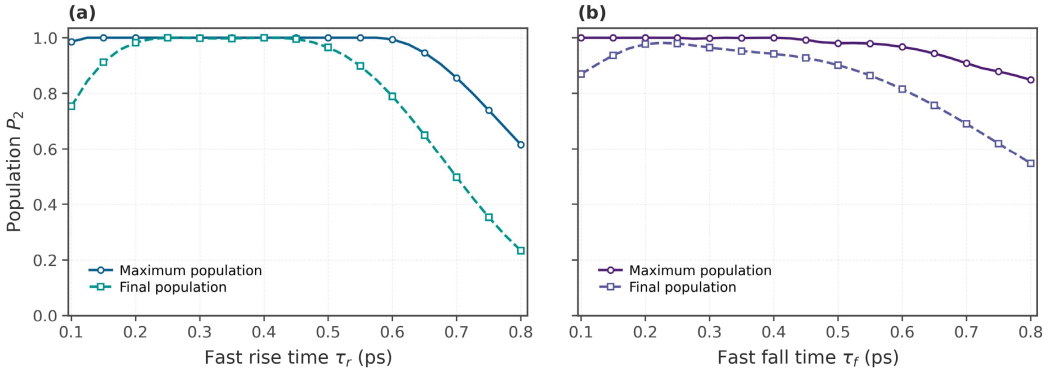


Figure 2. Target-state population as a function of the fast-edge duration. (**a**) RTST sequence as a function of the fast rise time τ_r, with $\tau_f = 8$ ps; (**b**) STRT sequence as a function of the fast fall time τ_f, with $\tau_r = 8$ ps. In both cases, the fast-edge duration is varied from 0.1 to 0.8 ps. The common pulse parameters are $t_0 = 32$ ps, $T_R = 55.24$ps, and $N = 5$. The solid and dashed curves denote the maximum and final target-state populations, respectively.

Figure 2b shows the corresponding results for the STRT pulse sequence, with the slow rise time τ_r fixed and the fast fall time τ_f optimized. The fast fall time τ_f was scanned from 0.1 ps to 0.8 ps. The maximum and final target-state populations are again plotted as functions of τ_f. Under the respective optimized conditions considered here, the RTST sequence reaches a slightly higher maximum final population than the STRT sequence. As τ_f increases, the final population varies nonmonotonically. A local maximum of about 98.173% occurs at $\tau_f = 0.225$ ps. In the STRT sequence, the rapid turn-off of the optical field can induce strong nonadiabatic transitions. When the field decreases abruptly, part of the population can be transferred undesirably to the nontarget state, reducing the population retained in the target state. Therefore, although optimizing τ_f at the specific point of 0.225 ps gives a relatively high value of 98.173%, the maximum final population remains slightly lower than the corresponding optimum obtained with the RTST sequence.

Figure 3a,b show the target-state population dynamics for a representative fast-edge duration of 0.2 ps, corresponding to $\tau_r = 0.2$ ps for RTST and $\tau_f = 0.2$ ps for STRT. Under RTST driving, the population exhibits a step-like increase (Figure 3a). The fast rise in each pulse produces nonadiabatic driving and a rapid step-like increase in the population, whereas the subsequent slow fall allows the field to turn off under approximately adiabatic conditions, producing a relatively flat plateau. The plateau height increases from pulse to pulse, leading to stepwise population accumulation. For a pulse number $N = 5$, the population approaches unity. In contrast, the STRT sequence shows markedly different dynamics (Figure 3b). The slow rise promotes adiabatic following, and the population increases smoothly as the field grows, enabling efficient population injection without a pronounced step-like feature. The subsequent finite fast-fall interval induces nonadiabatic population redistribution before the field is completely switched off. Once the field vanishes, the bare-state populations remain frozen in the coherent limit. Repeated pulses nevertheless continue to increase the target-state population in an overall stepwise trend, while the nonadiabatic redistribution associated with each fast-fall interval leads to a slightly lower final population than that obtained with RTST.

As shown in Figure 3c,d, when decoherence is included with a spontaneous decay rate $\gamma = 10^8 \mathrm{s}^{-1}$, the characteristic population dynamics of the asymmetric pulse sequences are retained, although the plateau heights decrease. This reduction arises from continuous spontaneous-emission loss from the excited state during the evolution, which lowers the population-accumulation efficiency. For $T = 300$ ps, $\gamma T = 0.03$, indicating that the calculations correspond to a weak-decay regime. Under these conditions, the final target-

state populations are $P_2^{\mathrm{RTST}}(T) \approx 0.9719$ and $P_2^{\mathrm{STRT}}(T) \approx 0.9638$, respectively. Despite the overall reduction, the distinct dynamical features associated with the slow fall of the RTST sequence and the rapid cutoff of the STRT sequence remain visible, with RTST retaining a slightly higher final target-state population. These results indicate that the characteristic population dynamics of both asymmetric pulse sequences are preserved under the weak-decay conditions considered here, while spontaneous emission reduces the final population-transfer efficiency.

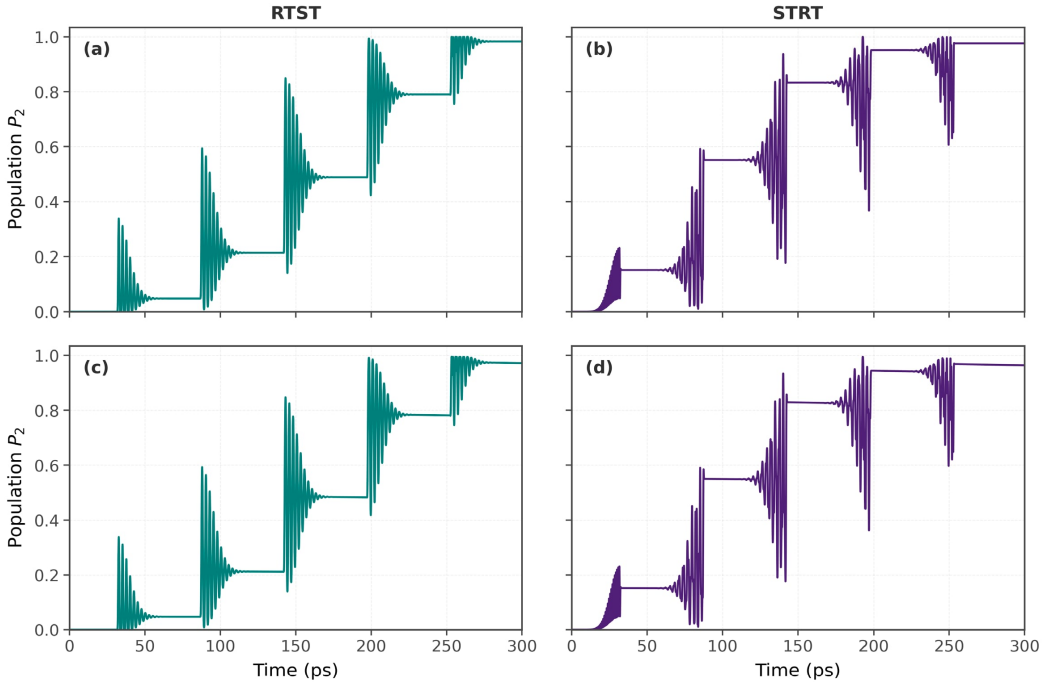


Figure 3. Population dynamics of the target state in a two-level system driven by asymmetric pulse sequences. The common parameters are $t_0 = 32$ ps, $T_R = 55.24$ ps and $N = 5$. (**a**) RTST sequence with $\tau_r = 0.2$ps and $\tau_f = 8$ ps; (**b**) STRT sequence with $\tau_r = 8$ ps and $\tau_f = 0.2$ ps; (**c**) RTST sequence in the presence of decoherence with $\tau_r = 0.2$ ps, $\tau_f = 8$ ps, and $\gamma = 10^8$ s^{-1}; (**d**) STRT sequence in the presence of decoherence with $\tau_r = 8$ ps, $\tau_f = 0.2$ ps, and $\gamma = 10^8$ s^{-1}.

We next examine the control fields associated with the CD-assisted protocols. Figure 4 compares the reference coupling, the CD quadrature, the resulting total control amplitude, and the corresponding phase correction for the RTST and STRT sequences. Here, the total transverse amplitude and phase correction are defined as $\Omega_{\mathrm{tot}}(t) = \sqrt{\Omega^2(t) + \Omega_{\mathrm{CD}}^2(t)}$ and $\delta\varphi(\mathrm{t}) = -\mathrm{atan2}[\Omega_{\mathrm{CD}}(t), \Omega(t)]$, respectively. The CD contribution remains smaller than the dominant reference coupling and is concentrated around the rapidly varying regions of the control trajectory, while the total transverse amplitude remains close to the reference pulse amplitude. The phase correction provides the additional quadrature required for implementing the CD-assisted control field.

The peak CD quadrature reaches approximately 1.03 rad ps^{-1} for RTST and 1.12 rad ps^{-1} for STRT, corresponding to approximately 20.5% and 22.3% of the reference peak coupling $\Omega_{\mathrm{peak}} = 5$ rad ps^{-1}, respectively. The apparent phase jumps occur near vanishing transverse amplitude and reflect the phase convention of the quadrature representation.

To show more directly how the CD correction modifies the experimentally relevant driving field, Figure 5 compares the laboratory-frame quadrature components with and without CD around the fast pulse edges. For RTST, the main correction appears during the fast-rising edge, whereas for STRT it is concentrated around the fast-falling edge. Away from these rapidly varying regions, the CD-corrected and reference fields nearly coincide.

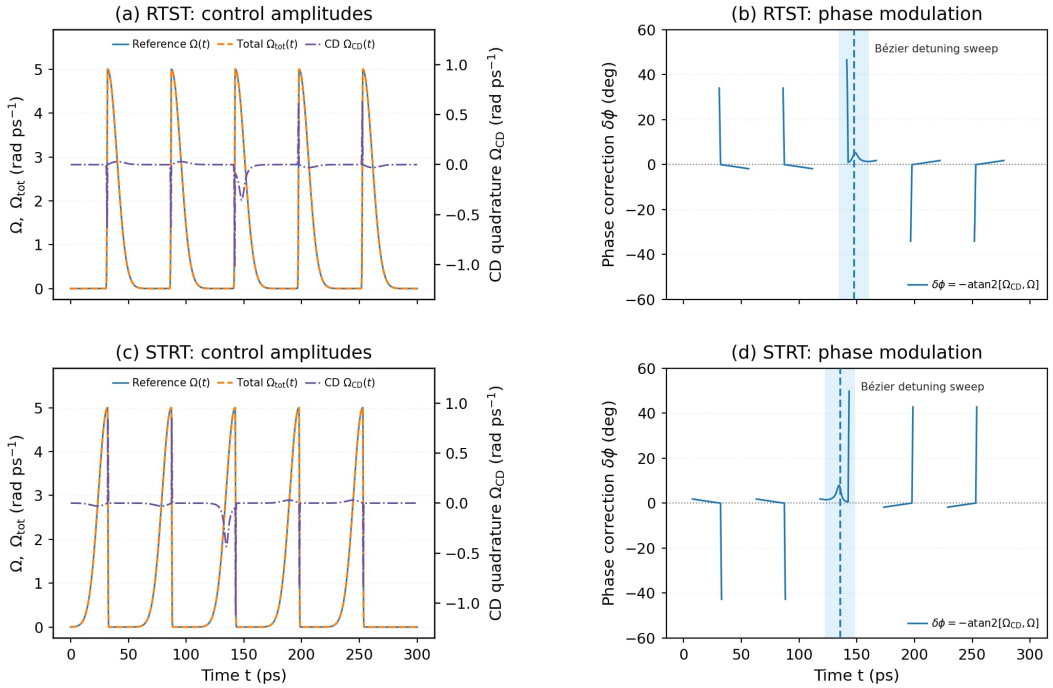


Figure 4. Counterdiabatic control amplitudes and phase modulation for the asymmetric pulse sequences. (**a**) Reference coupling $\Omega(t)$, total transverse amplitude $\Omega_{\mathrm{tot}}(t)$ (**left** axis), and CD quadrature $\Omega_{\mathrm{CD}}(t)$ (**right** axis) for RTST; (**b**) corresponding phase correction $\delta\varphi(t)$. Panels (**c**,**d**) show the corresponding results for STRT. The shaded regions in (**b**,**d**) indicate the finite-time Bézier detuning sweep.

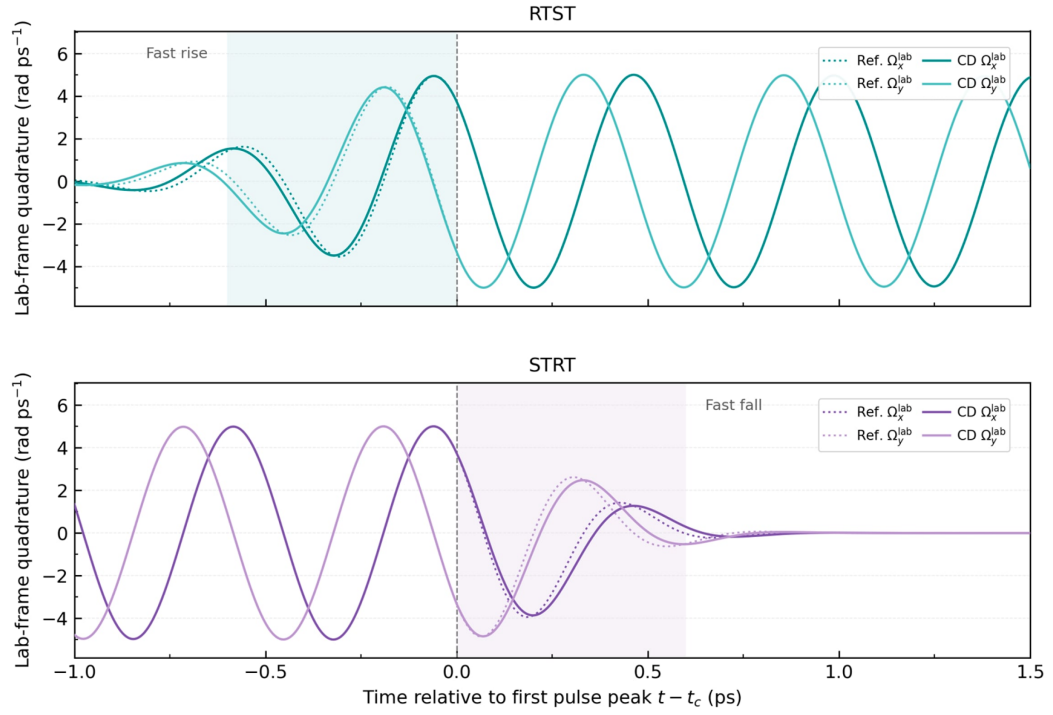


Figure 5. Laboratory-frame quadrature fields $\Omega_{\mathrm{x}}^{\mathrm{lab}}$ and $\Omega_{\mathrm{y}}^{\mathrm{lab}}$ around the fast edges of the RTST (**upper** panel) and STRT (**lower** panel) pulse sequences, where $\Omega_{\mathrm{x}}^{\mathrm{lab}}$ and $\Omega_{\mathrm{y}}^{\mathrm{lab}}$ denote the two orthogonal components of the laboratory-frame control field. The dotted curves denote the reference quadrature components, whereas the solid curves denote the corresponding CD-corrected fields. The shaded regions indicate the fast-rise interval for RTST and the fast-fall interval for STRT, respectively.

The required quadrature correction corresponds to a phase-controlled two-component drive and can, in principle, be generated using phase-locked quadrature synthesis or ultrafast amplitude-and-phase pulse-shaping techniques with sufficient sub-picosecond bandwidth.

To examine the dependence of the final-state fidelity on the pulse parameters, we map the fidelity in the parameter space spanned by the fast-edge time and the normalized field amplitude, as shown in Figure 6. In this analysis, the asymmetric coupling envelope $\Omega(t)$ is combined with the prescribed Bézier detuning sweep $\Delta(t)$ to define the reference Hamiltonian $H_0(t)$. The evolution without CD is governed by this reference Hamiltonian, whereas the CD-assisted evolution additionally incorporates $H_{\mathrm{CD}}(t)$, with the same reference trajectory retained in both cases. Thus, the comparison differs from the bare pulse-train dynamics in Figure 3, where no independent detuning sweep is introduced. Without CD, the final fidelity exhibits a clear dependence on the pulse parameters. With CD, the correction is recalculated for each parameter pair, leading to high final fidelities over a wider region of the scanned parameter space, with the representative operating points marked by the stars.

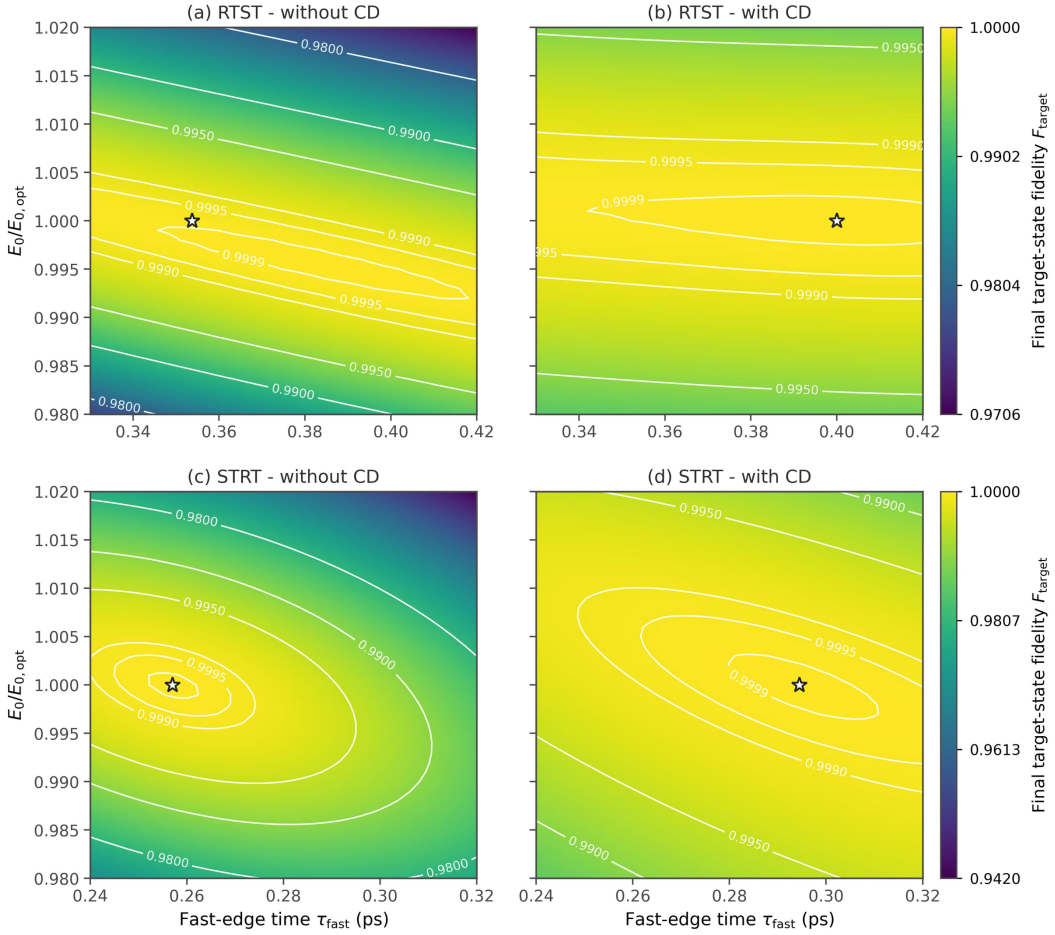


Figure 6. Final target-state fidelity $F_{\mathrm{target}} = P_2(T)$ as a function of the fast-edge time τ_{fast} and the normalized field amplitude $E_0/E_{0,\mathrm{opt}}$. Panels (**a**,**b**) show the RTST sequence without CD and with CD, respectively, while panels (**c**,**d**) show the corresponding results for the STRT sequence. The white contour lines indicate constant-fidelity levels, and the stars mark the representative optimized operating points.

To complement the final-state parameter analysis, Figure 7 shows the time-dependent infidelity $1 - F(t)$ for several representative fast-edge times under the same reference Hamiltonian used in Figure 6, with and without the CD term. Here, $F(t)$ denotes the instantaneous fidelity with respect to the reference eigenstate defined in Equation (13).

Without CD, pronounced infidelity peaks appear during the rapidly varying stages of the evolution, indicating transient deviations from the instantaneous reference eigenstate. In particular, the largest deviations occur near the characteristic sweep time t_c, where the control parameters vary most rapidly. After counterdiabatic driving is introduced, the corresponding infidelity is strongly suppressed from the 10^{-2} scale to the numerical-residual level. Under the adopted high-accuracy propagation, the residual infidelities with CD are displayed on a common 10^{-20} scale in the insets. Similar suppression is observed for both RTST and STRT sequences, demonstrating that the counterdiabatic correction effectively compensates the residual nonadiabatic coupling during the fast evolution.

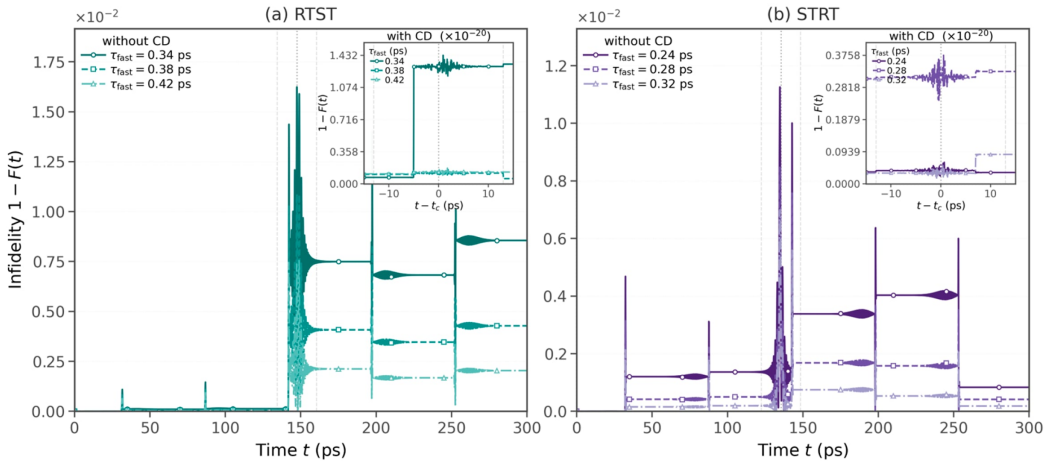


Figure 7. Time-dependent infidelity $1 - F(t)$ for representative fast-edge times. Panel (**a**) shows the RTST sequence and panel (**b**) shows the STRT sequence. The main panels show the results without CD over the full evolution, while the insets show the corresponding results with CD around the characteristic time t_c. The dotted vertical line marks t_c, and the dashed lines indicate the boundaries of the finite-time Bézier sweep. Counterdiabatic driving suppresses the infidelity from the 10^{-2} scale to the numerical-residual level; the results with CD in both insets are displayed on a common 10^{-20} scale.

4. Discussion

The results presented above show that the temporal asymmetry of the pulse envelope plays an important role in determining the population-transfer dynamics. Although both RTST and STRT sequences allow independent control of the fast and slow pulse edges, their dynamical responses are different. For RTST, the rapid turn-on establishes the coupling within a short time, whereas the subsequent slow turn-off reduces residual population oscillations and helps retain the accumulated population in the target state. For STRT, the slow turn-on produces a smoother initial population increase, while the finite fast-fall interval introduces stronger nonadiabatic population redistribution before the field is completely switched off. This difference accounts for the slightly higher optimized final population obtained with RTST in the bare asymmetric-pulse calculations. When spontaneous decay is included, the main dynamical features of both sequences remain visible, although the final populations decrease. Since the present calculations correspond to the weak-decay regime, these results should be interpreted as demonstrating preservation of the characteristic pulse-driven dynamics rather than general robustness against decoherence.

Previous studies have demonstrated the usefulness of asymmetric pulse sequences for population manipulation [55,56], while counterdiabatic and related shortcut-to-adiabaticity protocols have been developed for rapid population transfer in two- and three-level systems [58–60]. The present work combines these two control concepts. The asymmetric RTST/STRT envelope determines the temporal structure of the transverse coupling, whereas the prescribed detuning trajectory defines the reference path used for the CD construction.

Although exact counterdiabatic driving suppresses the nonadiabatic transitions associated with the reference Hamiltonian for either pulse envelope, the RTST/STRT asymmetry remains relevant to the structure of the required correction field. Since the CD term depends on the time derivatives of the reference control parameters, the rapid rising edge of RTST and the rapid falling edge of STRT lead to different temporal distributions and peak amplitudes of the CD correction. Thus, the asymmetric envelope primarily determines the timing and control-field requirements of the CD-assisted protocol, rather than providing an independent advantage in the ideal final-state fidelity once exact compensation is applied. The resulting CD term provides an additional orthogonal control component that compensates the nonadiabatic coupling generated during the finite-time evolution. As shown by the control-field analysis, the CD contribution is most pronounced near rapidly varying regions of the control trajectory and remains smaller than the dominant reference coupling. The corresponding laboratory-frame representation can therefore be expressed in terms of phase-controlled quadrature components, providing a direct connection between the theoretical CD construction and experimentally relevant amplitude-and-phase control.

The fidelity maps and time-dependent infidelity further clarify the role of the CD correction. Without CD, the final population and the instantaneous fidelity remain sensitive to the fast-edge duration and field amplitude because rapid parameter variation produces transient deviations from the prescribed reference eigenstate. With CD, these deviations are strongly suppressed and final fidelities above 0.99999 are obtained for both asymmetric protocols. It should be emphasized, however, that the CD correction in the parameter scans is recalculated for each parameter pair. Therefore, the broader high-fidelity regions characterize a family of parameter-matched CD-assisted protocols rather than the robustness of a single fixed CD waveform. Within this interpretation, the results show that accurate path compensation can maintain high-fidelity transfer over a wider range of the considered control parameters.

The present model also has several limitations. The analysis is based on a semiclassical two-level description, and the dissipative dynamics include spontaneous decay as the dominant loss channel. Additional effects, such as pure dephasing, stronger environmental coupling, multilevel structure, parameter mismatch, and finite experimental bandwidth, are not included explicitly. Moreover, the current CD-assisted parameter scans assume that the correction field is adjusted to the corresponding control trajectory. Future work may therefore examine the performance of a fixed or imperfect CD waveform under parameter uncertainty, as well as extend the method to multilevel systems and experimentally realistic pulse-shaping constraints. Such studies would further clarify the applicability of asymmetric-pulse-assisted counterdiabatic control to more complex quantum systems.

5. Conclusions

In this work, we combine asymmetric pulses with counterdiabatic driving to investigate fast and high-fidelity quantum-state manipulation. Through a theoretical model and systematic numerical simulations, we reveal the physical mechanisms by which the RTST and STRT pulse sequences produce population accumulation and show that their main dynamical features remain discernible under the weak-decay conditions considered, although spontaneous emission reduces the final populations. More importantly, by introducing the adiabatic gauge potential to construct the CD correction, we substantially suppress the nonadiabatic transitions associated with the asymmetric control paths. When the CD correction is recalculated for each parameter set, the resulting parameter-matched protocols yield final-state fidelities above 0.99999 for both asymmetric pulse sequences in the closed-system calculations. These results clarify the complementary roles of temporal pulse shaping and counterdiabatic path compensation in quantum control. This approach

provides an effective route to fast and high-fidelity quantum-state manipulation, with potential for extension to larger-scale atomic arrays [61,62] and prospective applications in quantum computing, quantum simulation, and quantum networks.

Author Contributions: Conceptualization, M.Y. and Y.Z.; methodology, M.Y. and Y.Z.; software, M.Y., X.L. and H.W.; validation, M.Y., X.L., H.W., X.Z. and Y.Z.; formal analysis, M.Y. and X.L.; investigation, M.Y. and Y.Z.; resources, Y.Z.; data curation, M.Y., X.L. and H.W.; writing—original draft preparation, M.Y.; writing—review and editing, M.Y., X.L., Z.B., M.F., R.G. and Y.Z.; visualization, M.Y., X.L. and H.W.; supervision, Y.Z.; project administration, Y.Z.; funding acquisition, Y.Z. All authors have read and agreed to the published version of the manuscript.

Funding: This study was supported by the Shanxi University's Training Program for Innovation for Undergraduates, the San Jin Enhancement Program for Outstanding Undergraduates of Shanxi University, the National Natural Science Foundation of China (Nos. 12574375 and 12004231), the Fundamental Research Program of Shanxi Province (Grant No. 202203021211301), and the Research Project Supported by Shanxi Scholarship Council of China (Nos. 2023-028 and 2022-014).

Institutional Review Board Statement: Not applicable.

Informed Consent Statement: Not applicable.

Data Availability Statement: The data and numerical codes supporting the conclusions of this article will be made available by the authors on request.

Conflicts of Interest: The authors declare no conflicts of interest.

References

1. Bason, M.G.; Viteau, M.; Malossi, N.; Huillery, P.; Arimondo, E.; Ciampini, D.; Fazio, R.; Giovannetti, V.; Mannella, R.; Morsch, O. High-fidelity quantum driving. *Nat. Phys.* **2012**, *8*, 147–152. [CrossRef]
2. Zhang, J.; Pagano, G.; Hess, P.W.; Kyprianidis, A.; Becker, P.; Kaplan, H.; Gorshkov, A.V.; Gong, Z.-X.; Monroe, C. Observation of a many-body dynamical phase transition with a 53-qubit quantum simulator. *Nature* **2017**, *551*, 601–604. [CrossRef] [PubMed]
3. Philips, S.G.J.; Mądzik, M.T.; Amitonov, S.V.; de Snoo, S.L.; Russ, M.; Kalhor, N.; Volk, C.; Lawrie, W.I.L.; Brousse, D.; Tryputen, L.; et al. Universal control of a six-qubit quantum processor in silicon. *Nature* **2022**, *609*, 919–924. [CrossRef] [PubMed]
4. Guo, S.-A.; Wu, Y.-K.; Ye, J.; Zhang, L.; Lian, W.-Q.; Yao, R.; Wang, Y.; Yan, R.-Y.; Yi, Y.-J.; Xu, Y.-L.; et al. A site-resolved two-dimensional quantum simulator with hundreds of trapped ions. *Nature* **2024**, *630*, 613–618. [CrossRef] [PubMed]
5. Farouk, A.M.; Beterov, I.I.; Xu, P.; Bergamini, S.; Ryabtsev, I.I. Parallel Implementation of $CNOT^N$ and C_2NOT^2 Gates via Homonuclear and Heteronuclear Förster Interactions of Rydberg Atoms. *Photonics* **2023**, *10*, 1280. [CrossRef]
6. Born, M.; Fock, V. Beweis des Adiabatensatzes. *Z. Phys.* **1928**, *51*, 165–180. [CrossRef]
7. Kuklinski, J.R.; Gaubatz, U.; Hioe, F.T.; Bergmann, K. Adiabatic population transfer in a three-level system driven by delayed laser pulses. *Phys. Rev. A* **1989**, *40*, 6741–6744. [CrossRef] [PubMed]
8. Gaubatz, U.; Rudecki, P.; Schiemann, S.; Bergmann, K. Population transfer between molecular vibrational levels by stimulated Raman scattering with partially overlapping laser fields. A new concept and experimental results. *J. Chem. Phys.* **1990**, *92*, 5363–5376. [CrossRef]
9. Zheng, W.; Zhang, Y.; Dong, Y.; Xu, J.; Wang, Z.; Wang, X.; Li, Y.; Lan, D.; Zhao, J.; Li, S.; et al. Optimal control of stimulated Raman adiabatic passage in a superconducting qudit. *npj Quantum Inf.* **2022**, *8*, 9. [CrossRef]
10. Chanda, N.; Patnaik, P.; Bhattacharyya, R. Optimal population transfer using adiabatic rapid passage in the presence of drive-induced dissipation. *Phys. Rev. A* **2023**, *107*, 063708. [CrossRef]
11. Li, K.Z.; Tian, J.Z.; Xiao, L.T. Optimal stimulated Raman adiabatic passage using the dynamical quantum geometric tensor. *Phys. Rev. A* **2024**, *109*, 022443. [CrossRef]
12. Xu, S.; Li, X.; Li, X.; Li, J.; Xue, M. Efficient generation of multiqubit entanglement states using rapid adiabatic passage. *Phys. Rev. A* **2024**, *110*, 023108. [CrossRef]
13. Gong, M.; Yu, M.; Chu, Y.; Chen, W.; Cao, Q.; Wang, N.; Cai, J.; Betzholz, R.; Giannelli, L. Two-photon-transition superadiabatic passage in a nitrogen-vacancy center in diamond. *Phys. Rev. A* **2024**, *109*, 032626. [CrossRef]
14. Vepsäläinen, A.; Danilin, S.; Paladino, E.; Falci, G.; Paraoanu, G.S. Quantum Control in Qutrit Systems Using Hybrid Rabi-STIRAP Pulses. *Photonics* **2016**, *3*, 62. [CrossRef]
15. Kuznetsova, E.; Pellegrini, P.; Côté, R.; Lukin, M.D.; Yelin, S.F. Formation of deeply bound molecules via chainwise adiabatic passage. *Phys. Rev. A* **2008**, *78*, 021402(R). [CrossRef]

16. Shi, W.; Malinovskaya, S. Implementation of a single femtosecond optical frequency comb for rovibrational cooling. *Phys. Rev. A* **2010**, *82*, 013407. [CrossRef]
17. Jakubetz, W. Limitations of STIRAP-like population transfer in extended systems: The three-level system embedded in a web of background states. *J. Chem. Phys.* **2012**, *137*, 224312. [CrossRef] [PubMed]
18. Coello Pérez, E.A.; Bonitati, J.; Lee, D.; Quaglioni, S.; Wendt, K.A. Quantum state preparation by adiabatic evolution with custom gates. *Phys. Rev. A* **2022**, *105*, 032403. [CrossRef]
19. Liu, X.-F.; Matsumoto, Y.; Fujita, T.; Ludwig, A.; Wieck, A.D.; Oiwa, A. Accelerated Adiabatic Passage of a Single Electron Spin Qubit in Quantum Dots. *Phys. Rev. Lett.* **2024**, *132*, 027002. [CrossRef] [PubMed]
20. Sterk, J.D.; Coakley, H.; Goldberg, J.; Hietala, V.; Lechtenberg, J.; McGuinness, H.; McMurtrey, D.; Parazzoli, L.P.; Van Der Wall, J.; Stick, D. Closed-loop optimization of fast trapped-ion shuttling with sub-quanta excitation. *npj Quantum Inf.* **2022**, *8*, 68. [CrossRef]
21. Hauck, S.H.; Stojanović, V.M. Coherent Atom Transport via Enhanced Shortcuts to Adiabaticity: Double-Well Optical Lattice. *Phys. Rev. Appl.* **2022**, *18*, 014016. [CrossRef]
22. Fallek, S.D.; Sandhu, V.S.; McGill, R.A.; Gray, J.M.; Tinkey, H.N.; Clark, C.R.; Brown, K.R. Rapid exchange cooling with trapped ions. *Nat. Commun.* **2024**, *15*, 1089. [CrossRef] [PubMed]
23. Liang, X.-H.; Wu, L.-A.; Wang, Z.-M. Optimally Controlled Non-Adiabatic Quantum State Transmission in the Presence of Quantum Noise. *Photonics* **2023**, *10*, 274. [CrossRef]
24. Stefanatos, D.; Ruths, J.; Li, J.-S. Frictionless atom cooling in harmonic traps: A time-optimal approach. *Phys. Rev. A* **2010**, *82*, 063422. [CrossRef]
25. Yin, Z.; Li, C.; Allcock, J.; Zheng, Y.; Gu, X.; Dai, M.; Zhang, S.; An, S. Shortcuts to adiabaticity for open systems in circuit quantum electrodynamics. *Nat. Commun.* **2022**, *13*, 188. [CrossRef] [PubMed]
26. Takahashi, K.; del Campo, A. Shortcuts to Adiabaticity in Krylov Space. *Phys. Rev. X* **2024**, *14*, 011032. [CrossRef]
27. Čepaitė, I.; Polkovnikov, A.; Daley, A.J.; Duncan, C.W. Counterdiabatic Optimized Local Driving. *PRX Quantum* **2023**, *4*, 010312. [CrossRef]
28. Schindler, P.M.; Bukov, M. Counterdiabatic Driving for Periodically Driven Systems. *Phys. Rev. Lett.* **2024**, *133*, 123402. [CrossRef] [PubMed]
29. Duncan, C.W. Exact counterdiabatic driving in finite topological lattice models. *Phys. Rev. B* **2024**, *109*, 245421. [CrossRef]
30. Niu, J.; Liu, B.-J.; Zhou, Y.; Yan, T.; Huang, W.; Liu, W.; Zhang, L.; Jia, H.; Liu, S.; Yung, M.-H.; et al. Customizable Quantum Control via Stimulated Raman User-Defined Passage. *Phys. Rev. Appl.* **2022**, *17*, 034056. [CrossRef]
31. Cárdenas-López, F.A.; Chen, X. Shortcuts to Adiabaticity for Fast Qubit Readout in Circuit Quantum Electrodynamics. *Phys. Rev. Appl.* **2022**, *18*, 034010. [CrossRef]
32. Zhu, J.-J.; Guérin, S. Control of nonlinear quantum systems: From nonlinear Rabi oscillations to robust two-stage optimal inverse engineering. *Phys. Rev. A* **2024**, *110*, 063503. [CrossRef]
33. Chen, S.-Q.; Lu, H. Experimental acceleration of the spin transition in a nitrogen-vacancy center. *Phys. Rev. Appl.* **2025**, *23*, 024015. [CrossRef]
34. Chen, X.; Torrontegui, E.; Muga, J.G. Lewis-Riesenfeld invariants and transitionless quantum driving. *Phys. Rev. A* **2011**, *83*, 062116. [CrossRef]
35. Masuda, S.; Koenig, J.; Steele, G.A. Acceleration and deceleration of quantum dynamics based on inter-trajectory travel with fast-forward scaling theory. *Sci. Rep.* **2022**, *12*, 10744. [CrossRef] [PubMed]
36. Hatomura, T. Time rescaling of nonadiabatic transitions. *SciPost Phys.* **2023**, *15*, 036. [CrossRef]
37. Sauvage, F.; Mintert, F. Optimal Control of Families of Quantum Gates. *Phys. Rev. Lett.* **2022**, *129*, 050507. [CrossRef] [PubMed]
38. Chen, Q.-M.; Rabitz, H.; Wu, R.-B. Quantum optimal control without arbitrary waveform generators. *Phys. Rev. Appl.* **2023**, *20*, 064016. [CrossRef]
39. Shao, B.; Yang, X.; Liu, R.; Zhai, Y.; Lu, D.; Xin, T.; Li, J. Multiple classical noise mitigation by multiobjective robust quantum optimal control. *Phys. Rev. Appl.* **2024**, *21*, 034042. [CrossRef]
40. Petruhanov, V.N.; Pechen, A.N. Quantum Gate Generation in Two-Level Open Quantum Systems by Coherent and Incoherent Photons Found with Gradient Search. *Photonics* **2023**, *10*, 220. [CrossRef]
41. Berry, M.V. Transitionless quantum driving. *J. Phys. A Math. Theor.* **2009**, *42*, 365303. [CrossRef]
42. Demirplak, M.; Rice, S.A. Adiabatic Population Transfer with Control Fields. *J. Phys. Chem. A* **2003**, *107*, 9937–9945. [CrossRef]
43. Demirplak, M.; Rice, S.A. Assisted Adiabatic Passage Revisited. *J. Phys. Chem. B* **2005**, *109*, 6838–6844. [CrossRef] [PubMed]
44. Demirplak, M.; Rice, S.A. On the consistency, extremal, and global properties of counterdiabatic fields. *J. Chem. Phys.* **2008**, *129*, 154111. [CrossRef] [PubMed]
45. Chandarana, P.; Paul, K.; Garcia-de-Andoin, M.; Ban, Y.; Sanz, M.; Chen, X. Photonic counterdiabatic quantum optimization algorithm. *Commun. Phys.* **2024**, *7*, 315. [CrossRef]

46. Malla, R.K.; Sukeno, H.; Yu, H.; Wei, T.-C.; Weichselbaum, A.; Konik, R.M. Feedback-based quantum algorithm inspired by counterdiabatic driving. *Phys. Rev. Res.* **2024**, *6*, 043068. [CrossRef]
47. van Vreumingen, D. Gate-based counterdiabatic driving with complexity guarantees. *Phys. Rev. A* **2024**, *110*, 052419. [CrossRef]
48. Mahunta, S.; Mukherjee, V. Shortcuts to adiabaticity in open quantum critical systems. *Phys. Rev. B* **2025**, *111*, 064301. [CrossRef]
49. Dengis, S.; Wimberger, S.; Schlagheck, P. Accelerated creation of NOON states with ultracold atoms via counterdiabatic driving. *Phys. Rev. A* **2025**, *111*, L031301. [CrossRef]
50. Wang, X.; Fan, H.; Bai, Z.; Zhang, Y. Geometric quantum gates of non-closed paths under counterdiabatic driving. *Appl. Phys. Lett.* **2026**, *128*, 094002. [CrossRef]
51. Chathanathil, J.; Ramaswamy, A.; Malinovsky, V.S.; Budker, D.; Malinovskaya, S.A. Chirped fractional stimulated Raman adiabatic passage. *Phys. Rev. A* **2023**, *108*, 043710. [CrossRef]
52. Güngördü, U.; Kestner, J.P. Robust quantum gates using smooth pulses and physics-informed neural networks. *Phys. Rev. Res.* **2022**, *4*, 023155. [CrossRef]
53. Kuzmanović, M.; Björkman, I.; McCord, J.J.; Dogra, S.; Paraoanu, G.S. High-fidelity robust qubit control by phase-modulated pulses. *Phys. Rev. Res.* **2024**, *6*, 013188. [CrossRef]
54. Collins, T.A.; Malinovskaya, S.A. Manipulation of ultracold Rb atoms using a single linearly chirped laser pulse. *Opt. Lett.* **2012**, *37*, 2298–2300. [CrossRef] [PubMed]
55. Zhang, W.; Wang, G.-R.; Cong, S.-L. Efficient photoassociation with a train of asymmetric laser pulses. *Phys. Rev. A* **2011**, *83*, 045401. [CrossRef]
56. Zhang, Y.; Bai, Z.; Fan, H.; Wang, X. Spectral Shaping of an Optical Frequency Comb to Control Atomic Dynamics. *Photonics* **2025**, *12*, 1015. [CrossRef]
57. Lasek, A.; Lepage, H.V.; Zhang, K.; Ferrus, T.; Barnes, C.H.W. Pulse-controlled qubit in semiconductor double quantum dots. *Sci. Rep.* **2023**, *13*, 21369. [CrossRef] [PubMed]
58. Chen, X.; Lizuain, I.; Ruschhaupt, A.; Guéry-Odelin, D.; Muga, J.G. Shortcut to Adiabatic Passage in Two- and Three-Level Atoms. *Phys. Rev. Lett.* **2010**, *105*, 123003. [CrossRef] [PubMed]
59. Ibáñez, S.; Chen, X.; Torrontegui, E.; Muga, J.G.; Ruschhaupt, A. Multiple Schrödinger Pictures and Dynamics in Shortcuts to Adiabaticity. *Phys. Rev. Lett.* **2012**, *109*, 100403. [CrossRef] [PubMed]
60. Kosionis, S.G.; Biswas, S.; Fouseki, C.; Stefanatos, D.; Paspalakis, E. Efficient Population Transfer in a Quantum Dot Exciton under Phonon-Induced Decoherence via Shortcuts to Adiabaticity. *Phys. Rev. B* **2025**, *112*, 075304. [CrossRef]
61. Mizoguchi, M.; Zhang, Y.; Kunimi, M.; Tanaka, A.; Takeda, S.; Takei, N.; Bharti, V.; Koyasu, K.; Kishimoto, T.; Jaksch, D.; et al. Ultrafast Creation of Overlapping Rydberg Electrons in an Atomic BEC and Mott-Insulator Lattice. *Phys. Rev. Lett.* **2020**, *124*, 253201. [CrossRef] [PubMed]
62. Bharti, V.; Sugawa, S.; Mizoguchi, M.; Kunimi, M.; Zhang, Y.; de Léséleuc, S.; Tomita, T.; Franz, T.; Weidemüller, M.; Ohmori, K. Picosecond-Scale Ultrafast Many-Body Dynamics in an Ultracold Rydberg-Excited Atomic Mott Insulator. *Phys. Rev. Lett.* **2023**, *131*, 123201. [CrossRef] [PubMed]

Disclaimer/Publisher's Note: The statements, opinions and data contained in all publications are solely those of the individual author(s) and contributor(s) and not of MDPI and/or the editor(s). MDPI and/or the editor(s) disclaim responsibility for any injury to people or property resulting from any ideas, methods, instructions or products referred to in the content.